Electrochimica Acta 536 (2025) 146707

Contents lists available at ScienceDirect

Electrochimica Acta

journal homepage: www.journals.elsevier.com/electrochimica-acta

Performance and stability of PtCo alloy catalysts in high-temperature polymer electrolyte membrane fuel cells

V. Domin [a], M. Prokop [a,*], T. Bystron [a], M. Gatalo [b,c], L. Pavko [b,c], N. Hodnik [b], B.F. Gomes [d], C.M.S. Lobo [d], C.E. Hartwig [d], C. Roth [d], M. Paidar [a], K. Bouzek [a]

[a] Department of Inorganic Technology, University of Chemistry and Technology Prague, Technicka 5, Prague 6, 166 28, Czech Republic
[b] Department of Materials Chemistry, National Institute of Chemistry, Hajdrihova 19, p.p. 660, Ljubljana SI-1001, Slovenija
[c] ReCatalyst d.o.o., Hajdrihova Ulica 19, Ljubljana 1000, Slovenia
[d] Electrochemical Process Engineering, University of Bayreuth, Universitätsstraße 30, Bayreuth 95447, Germany

ARTICLE INFO

Keywords:
High-temperature PEM fuel cell
Pt catalyst
Intermetallic alloy
Catalyst support
Reduced graphene oxide

ABSTRACT

High-temperature polymer electrolyte membrane fuel cells (HT-PEMFCs) suffer from fast catalyst degradation and catalyst poisoning by phosphate anions. Their performance can be tuned by alloying Pt with a less noble metal and by choosing an appropriate catalyst support and preparation method. To address this, we investigate the performance of two novel PtCo intermetallic alloy catalysts supported either on carbon black or reduced graphene oxide (rGO), prepared by double passivation galvanic displacement method, appropriate thermal annealing and *ex situ* chemical activation. The catalysts were used on the cathode and/or anode of a single cell (H_2/O_2, 180 °C, 144 h) to shed light on the Co lifecycle in HT-PEMFCs. *I-U* curves as well as electrochemical impedance spectroscopy showed that their use on the cathode improved cell performance, partly also due to Co dissolution, providing higher surface area and more active sites. On the other hand, when they were used on the anode and on both electrodes, the cell performance was marked by severely inhibited mass transport due to Co phosphate formation. XRF and XAS showed that regardless of where a PtCo catalyst is used, Co at least partly dissolves and is transported to the other electrode, affecting the cell performance.

List of abbreviations

CB	carbon black
CL	catalyst layer
CNC	computer numerical control
DMF	N,N-dimethylformamide
ECSA	electrochemically active surface area, in italics as a physical quantity
$ECSA_{HUPD}$	electrochemically active surface area measured by hydrogen underpotential deposition
$ECSA_{CO}$	electrochemically active surface area measured by CO stripping
EIS	electrochemical impedance spectroscopy
EXAFS	extended X-ray absorption fine structure
FC	fuel cell
GDE	gas diffusion electrode
GDL	gas diffusion layer
HOR	H_2 oxidation reaction
HT	high-temperature
H_{UPD}	hydrogen underpotential deposition
KB	Ketjenblack
MEA	membrane electrode assembly
NP	nanoparticle
ORR	O_2 reduction reaction
PBI	polybenzimidazole
PEMFC	polymer electrolyte membrane fuel cell
PTFE	polytetrafluorethylene
rGO	reduced graphene oxide
SI	supplementary information
XANES	X-ray absorption near edge structure
XAS	X-ray absorption spectroscopy
XRD	X-ray diffraction
XRF	X-ray fluorescence

1. Introduction

High-temperature polymer electrolyte membrane fuel cells (HT-PEMFCs) operate within the temperature range of 120 to 200 °C and primarily utilise membranes based on polybenzimidazole (PBI) or its

* Corresponding author.
E-mail address: prokopm@vscht.cz (M. Prokop).

https://doi.org/10.1016/j.electacta.2025.146707
Received 28 March 2025; Received in revised form 4 June 2025; Accepted 11 June 2025
Available online 12 June 2025

derivatives and doped with H_3PO_4 to maintain proton conductivity [1]. These operating temperatures enable efficient heat recovery during operation, making HT-PEMFCs suitable for the micro-cogeneration of heat and power. Additionally, HT-PEMFCs are resistant to CO poisoning up to 5 vol.% [2,3], which enables coupling with internal reformers, thereby enhancing their versatility for micro-cogeneration or auxiliary power units [4]. However, HT-PEMFCs suffer from drawbacks, such as requiring high Pt loading due to Pt nanoparticle (NP) degradation and susceptibility to H_3PO_4 poisoning [5,6]. These problems can be at least partially alleviated by the use of a suitable Pt alloy catalyst and catalyst support [7].

Several Pt alloys have been researched as HT-PEMFC catalysts. Of these, PtCu, PtNi and PtCo have garnered attention. PtCu [8,9] and PtNi [10] catalysts were not only reported to possess higher catalytic activity to the oxygen reduction reaction (ORR) than pure Pt due to the alloying effects but also showed more resilience to phosphate anion poisoning. PtCo catalysts exhibit higher ORR activity in H_3PO_4, and can compete with commercial Pt/C catalysts, even at lower Pt loadings [11]. Furthermore, PtCo alloys have demonstrated long-term performance similar to that of commercial Pt catalysts. Despite this, stability remains an issue of alloy catalysts [12].

In addition to tuning catalyst activity by alloying Pt with a less noble metal, various carbon supports, and modifications thereof, have also attracted researcher attention. In particular, graphene and related materials offer a wide range of possible catalyst supports, mainly due to their stability and high electronic conductivity [13]. Reduced graphene oxide (rGO), albeit not widely researched as a catalyst support for HT-PEMFCs, has shown high stability and improved resistance to the loss of electrochemically active surface area (ECSA) of the catalyst, as well as allowing similar catalyst activity as carbon blacks (CBs) [14,15]. Graphene nanoplatelets have also exhibited better stability and performance than CBs [13]. Among other widely researched materials, carbon nanotubes appear to be highly durable against Pt-catalysed corrosion [16]. Furthermore, Pt nanoparticles deposited on such nanotubes have shown better resistance to ECSA loss and higher peak power densities than Pt/CB [17]. Oxidising carbon nanotubes to introduce carboxyl groups and coating the resulting catalyst material with PBI after nanoparticle deposition can result in enhanced degradation resistance and proton conduction [18].

Together with the selected catalyst support, the manufacturing method of a Pt alloy catalyst also has a significant effect on its stability and activity. Typically, catalysts have been prepared by the chemical reduction of metal precursors with a change in pH [11]. Later, galvanic displacement of the less noble metal started being used [19,20]. Based on this method, Gatalo *et al.* developed a three-step procedure, consisting of galvanic displacement of the sacrificial metal [21], thermal annealing of the catalyst nanoparticles [22], and *ex situ* chemical activation to reduce the amount of the less noble metal in the surface layer [23]. The advantages of this procedure are that it is scalable and can proceed in water at ambient temperature. Moreover, such-prepared catalysts have shown good catalytic properties to the ORR on various supports when used in low-temperature PEMFCs [21,24]. However, their use in HT-PEMFCs has not yet been examined.

It is clear that Pt nanoparticular catalysts on CB support are reaching their technological limits in HT-PEMFCs and there is an urgent need to introduce novel, stable, and active catalysts to improve overall cell performance and durability. The main target of this study is thus to assess the potential application of novel bimetallic catalysts (PtCo produced by the galvanic displacement method on either rGO or CB) and provide insight into their behaviour in the HT-PEMFC anode and/or cathode.

2. Experimental

2.1. Materials and chemicals

Chemicals used in this work were: 85 wt.% H_3PO_4 (Acros Organics, extra pure), 30 wt.% H_2O_2 (Lach-Ner, per analysis, unstabilised), N,N-dimethylformamide (Penta, per analysis), and 10 wt.% PBI solution in N,N-dimethylformamide (PBI Performance products). Gases used were O_2 (99.5 %, SIAD), N_2 (99.99 %, SIAD), H_2 (99.999 %, SIAD), and CO (99 %, SIAD). Deionised water (conductivity 1.3 μS cm^{-1}) used during the work was prepared by DIWA 3rica system (WATEK, Czechia).

Since even extra pure grade of commercially available H_3PO_4 contains non-negligible amount of H_3PO_3, which adsorbs strongly on Pt surface and blocks active sites on the electrodes [25,26], H_3PO_4 was purified by heating with H_2O_2. In particular, 85 wt.% H_3PO_4 was mixed with H_2O_2 in the volumetric ratio of 2:1. The mixture was poured in a polytetrafluorethylene (PTFE) container and heated to 120 ℃ at which temperature the oxidation of P species (oxidation state $< +5$), decomposition of H_2O_2 (exothermic) takes place. After 15 min at 120 ℃, the solution was heated to 160 ℃ and left at this temperature for 24 h to remove remaining water. The as-prepared solution was poured in a glass storage bottle while still hot not to absorb water from the air in the meantime.

The membranes used in the experiments were TPS® (pyridine containing copolymers of poly(ether sulfone) and tetramethyl biphenyl groups, Advent). Gas diffusion layer (GDL) Sigracet 38BC® (SGL) was used for electrode preparation. Three types of catalysts were used – commercial HiSPEC 4000® with nominally 40 wt.% of Pt (Pt/C) on carbon black Vulcan XC-72 (Johnson Matthey) and two experimental ones, one with 30.7 wt.% of Pt and 3 wt.% of Co on reduced graphene oxide (PtCo/rGO) [27] and one with 31.2 wt.% Pt and 1.9 wt.% Co on carbon black Ketjenblack® EC300J (PtCo/KB) [28,29].

2.2. Catalyst preparation

PtCo catalysts used in this work were provided by the National Institute of Chemistry (PtCo/rGO) and ReCatalyst (PtCo/KB). Their preparation process, described in detail in [21,27–29], is briefly described in this text below.

2.3. Graphene oxide synthesis

Before the preparation of the catalysts themselves, graphene oxide (GO) was synthesised according to the modified Hummers' method [30]. 1 dm^3 of 96 wt.% Suprapur® H_2SO_4 (Merck) was mixed with 110 cm^3 of 85 wt.% H_3PO_4 in a 5 dm^3 beaker. Graphite (Imerys) was added afterwards and was followed by regular additions of 99.9 wt.% $KMnO_4$ (Carlo Erba) every 24 h to the total of 5 times the mass of GO. The mixture was stirred for two days, after that, the reaction was suppressed by ice and the gradual addition of 30 wt.% H_2O_2 (Belinka). These additions were stopped when the colour changed from violet to yellow. The GO was left to settle, and the liquid part of the mixture was replaced with ultrapure water. From then on, thus prepared GO was washed by dispersing it in 5 wt.% HCl (Carlo Erba), centrifugating, and re-dispersing in ultrapure water multiple times. In the last step of the synthesis, the GO suspension was homogenised in an ice bath for 1 h.

2.4. PtCo catalyst synthesis

With the use of a previously reported pulse combustion reactor [29], composite materials of Co supported either on carbon black Ketjenblack (KB) – Co/KB – or on reduced graphene oxide (rGO) – Co/rGO – were synthesised. For the Co/KB composite, 75.4 g of 99.9 wt.% Co $(AcO)_2{\cdot}4H_2O$ (Sigma Aldrich) and 30 g of Ketjenblack EC300J (Nouryon) were mixed in 1 dm^3 of ultrapure water. For Co/rGO, 25.0 g of $Co(AcO)_2{\cdot}4H_2O$ was dissolved in 1 dm^3 of a suspension containing

approximately 14 g of GO. These precursors were homogenised by thorough mixing for 10 min before being introduced into the pulse combustion reactor.

The reactor is equipped with a specialised combustor. Air flows in the combustor through a blower-powered valve, with airflow measured by a thermal mass flow meter. Another set of a mass flow meter and a controller regulates the fuel, C_3H_8, flow with the correct fuel-to-air ratio being achieved by adjusting the blower speed or fuel flow. Furthermore, to control pressure changes in the reactor, which affect temperature and gas composition, C_3H_8 can be mixed with N_2, leading to more efficient fuel combustion with less O_2. C_2H_2 can be injected in the combustor through a secondary inlet to improve the reductive atmosphere. Catalyst precursors are sprayed into the reactor's hot zone via a T-section. In the reactor, NPs form on the KB or rGO support due to the introduction of the precursors to the flue gas. Such prepared composite materials are collected using an electrostatic filter.

Using the previously reported double passivation galvanic displacement method [21], the PtCo intermetallic catalysts were prepared by the deposition of Pt NPs on the previously prepared Co/KB and Co/rGO. After the deposition, the materials were thermally annealed in Ar atmosphere for 5 h at the temperature of 700 °C to form the intermetallic crystal phase. As the last step of the synthesis, the catalysts were chemically activated, involving acid treatment and multiple washing cycles, according to standard procedures [31].

2.5. MEA preparation

Gas diffusion electrode (GDE) preparation was based on the procedure used by Prokop *et al.* [32]. Firstly, a catalyst ink was prepared. A catalyst material was poured into a 25 cm^3 vial, N, N-dimethylformamide (DMF) was added and then the PBI solution. The exact amounts of these compounds are shown in Table 1.

This mixture was ultrasonicated with an ultrasonic probe MS73 (Bandelin) with power output of 15 W for 10 min. Using a computer numerical control (CNC) sprayer with an ultrasonic head (CNC platform by CZRobotics, ultrasonic spray system by Cheersonic), the resulting ink was deposited on a square piece of GDL (10 × 10 cm^2) placed on a hot plate heated to 110 ℃. After spraying, the temperature of the hot plate was increased to 190 ℃ for 30 min. Consequently, the prepared GDE was left to cool down on the hot plate and placed in a dry box. Catalyst loading was controlled by comparing the GDL mass with the mass of prepared GDE, both measured on analytical scales MS304TS (Mettler-Toledo).

First, the membrane (3.5 × 3.5 cm^2) was doped according to the procedure recommended by the manufacturer by immersing it in 23 cm^3 of 85 wt.% H_3PO_4 (prepared by diluting the purified ~95 wt.% H_3PO_4 – see Section 2.1 – with deionised water) in a PTFE container with pins to keep the membrane submerged. The container with the membrane was placed in an oven (Falc) and the temperature was set to 120 ℃ for 20 h. After removing the membrane from the container, excess H_3PO_4 was removed from the membrane surface by pressing it between two PVC diaphragms (applied pressure of 1.2 kPa) for one minute. The overview of individual membrane electrode assembly (MEA) composition and their abbreviations used in the text are provided in Table 2.

Table 1
Composition of the experimental inks used for catalyst layer preparation: catalyst mass m_{cat}, mass of the 10 wt.% PBI solution m_{PBIsol}, and the volume of DMF V_{DMF}.

Catalyst	m_{cat} g	m_{PBIsol} g	V_{DMF} cm^3
Pt/C	0.251	0.279	17.72
PtCo/KB	0.265	0.294	18.71
PtCo/rGO	0.259	0.288	18.30

Table 2
MEAs used in the scope of this work with the description of conducted experiments and electrode loadings.

MEA code	Catalyst		Cathode loading mg cm^{-2}		Anode loading mg cm^{-2}	
	Cathode	Anode	metal	Pt	metal	Pt
MEA KBc	PtCo/KB	Pt/C	0.49	0.46	0.33	0.33
MEA KBa	Pt/C	PtCo/KB	0.33	0.33	0.49	0.46
MEA KBb	PtCo/KB	PtCo/KB	0.49	0.46	0.49	0.46
MEA rGOc	PtCo/rGO	Pt/C	0.45	0.41	0.33	0.33
MEA rGOa	Pt/C	PtCo/rGO	0.33	0.33	0.45	0.41
MEA rGOb	PtCo/rGO	PtCo/rGO	0.45	0.41	0.45	0.41
MEA C	Pt/C	Pt/C	0.33	0.33	0.33	0.33

2.6. Single cell experiments

An in-house crafted single cell with an active area of 6.25 cm^2 was used. Four screws (M6, torque of 5 N m) were then used to tighten the cell. The assembled cell was heated to 120 ℃ while being flushed with N_2 (flow of 50 cm^3 min^{-1} in each electrode compartment). After the temperature reached 120 ℃, N_2 flow was stopped and H_2 was introduced on the anode and O_2 on the cathode (36 cm^3 min^{-1}). The temperature and cell voltage were then set to 180 ℃ and 0.5 V, respectively. When the temperature and current stabilised, the mode was changed to galvanostatic at a current density of 0.5 A cm^{-2} (3.13 A) and corresponding flow of gases in stoichiometric excess of 50 % for H_2 and 100 % for O_2 were set, i.e. both at 36 cm^3 min^{-1}. These operating conditions were used for the cell break-in, lasting 24 h. Break-in was necessary for the stabilisation of the cell performance before application of testing protocol. O_2 was used instead of air in order to mitigate mass transfer limitations in the cell and to minimise negative effects of MEA drying, leading to faster stabilisation of performance between characterisation procedures.

Cell characterisation started after 24 h of break-in procedure, following the testing protocol described below:

- OCV acquisition for 30 s;
- a dynamic load curve for Tafel analysis was recorded in the potential range from OCV (around 1 V) to 0.3 V with a scan rate of 5 mV s^{-1} at a constant H_2 and O_2 flow rate of 100 cm^3 min^{-1};
- second OCV acquisition for 30 s followed by a second load curve was performed using the same settings as above;
- the electrochemical impedance spectroscopy (EIS) sequence was initiated. The spectra were recorded at voltages of 0.9, 0.8, 0.7, 0.6, 0.5, and 0.4 V after a 120 s long stabilisation period at any given voltage. Spectra were recorded for the frequency range of 18 kHz to 100 mHz with an amplitude of the perturbing signal of 10 mV. *I-U* data collected during the stabilisation period were used to construct the stationary load and power density curves. During each EIS measurement, a constant λ (stoichiometric excess of reactants) was maintained for all the voltages studied. EIS data were evaluated using an equivalent circuit (shown in Fig. S1) with Ohmic resistance and two (or three, in specific cases) time constants (detailed description of fitting procedure is included in Supplementary Information (SI), Section S1);
- hydrogen underpotential deposition (H_{UPD}) was performed twice to determine the changes in catalyst active surface (a detailed description of this type of measurement is given in Section S2 in SI);
- CO chemisorption was performed twice to determine the changes in catalyst active surface (a detailed description of this type of measurement is given in Section S2 in the SI);
- the tests were repeated again 72 and 144 h after the experiment start.

A list of tested MEAs and their description is provided in Table 2. In their names, a, b and c stand for anode, both electrodes and cath ode signalling where the PtCo catalysts were used. The catalysts themselves

are named according to their support: KB for PtCo/KB, rGO for PtCo/rGO and C for Pt/C.

Fig. S2 in the SI reports the mass of the membranes used in the respective MEAs before (m_{before}) and after (m_{after}) doping with H_3PO_4 and shows that the average doping level (m_{after}/m_{before}) of membranes used for MEA fabrication to be equal to 3.15 ± 0.29.

2.7. Ex situ analysis

For the post-mortem analyses, the electrodes from the used MEAs were delaminated from the membranes. During the X-ray diffraction (XRD) and X-ray fluorescence (XRF) measurements, the membranes were examined from both sides and electrodes only from the membrane side, schematically shown in Fig. S3 in SI. XRD measurements of the PtCo and commercial HiSPEC 4000 samples were performed on a High-resolution powder X-ray diffractometer X'Pert PRO (Malvern Panalytical). All other samples were characterised on the X'Pert3 Powder diffractometer (Malvern Panalytical). In both cases, the samples were placed on Si holders and a Cu anode was used (Kα radiation wavelength = 0.15418 nm). The average crystallite size of metallic nanoparticles was evaluated in the HighScore Plus software by the Scherrer equation. The Pt:Co ratios in the samples were examined by means of XRF using Axios XRF spectrometer (Malvern Panalytical) using a Rh lamp and a 4 kW generator.

The post-mortem X-ray absorption spectroscopy (XAS) measurements were performed at the P65 beamline of the PETRA III synchrotron radiation facility at the German Electron Synchrotron (DESY) in Hamburg, Germany. The measurements were performed in fluorescence

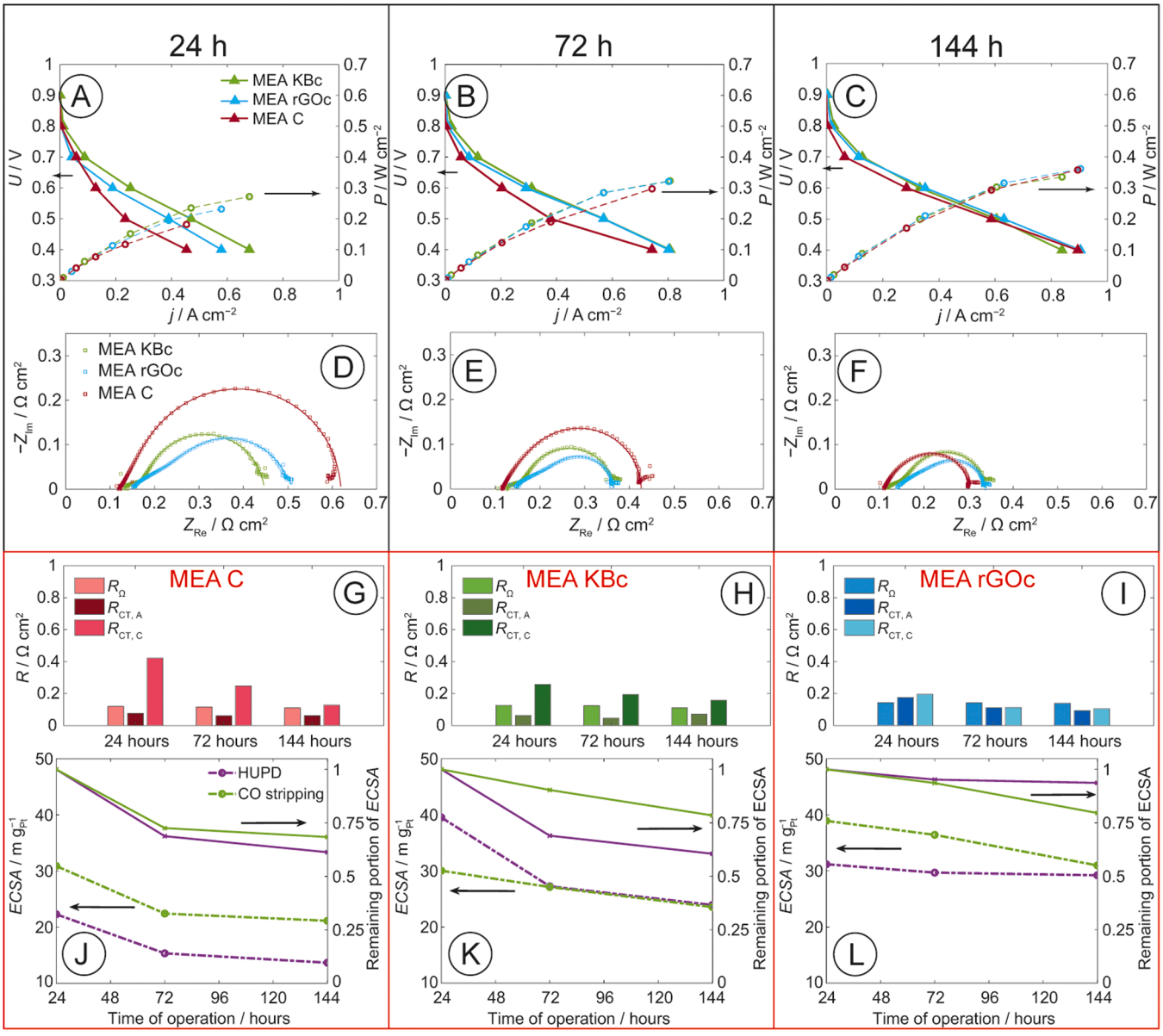

Fig. 1. Results of the testing protocol for MEAs with Pt/C on the anode and various catalysts on the cathode side of the fuel cell, see plot inset. A, B, C – stationary load and power density curves measured after 24, 72, and 144 h of operation, respectively; D, E, F – corresponding impedance spectra recorded at a voltage of 0.5 V, voltage amplitude was 10 mV, MEA C with Pt/C for comparison; G, H, I – bar graphs of the resistance of MEAs obtained by EIS spectra fitting; J, K, L – *ECSA* (dash-dotted lines) and the respective remaining portions of *ECSA* relating to the first measurement (thinner, dashed lines) obtained using H_{UPD} and CO stripping analyses. R_Ω is the ohmic resistance, $R_{CT,A}$ and $R_{CT,C}$ are the charge transfer resistances of the anode and cathode, respectively. In these graphs, KBc symbolises the MEA with PtCo/KB on the cathode, rGOc stands for the MEA with PtCo/rGO on the cathode and MEA C stands for Pt/C on the cathode. All three MEAs utilise Pt/C on the anode. More information can be found in Table 2.

(PIPS detector) and transmission mode. Spectra were collected at the Pt L_3-edge and Co K-edge. Metallic foils were measured simultaneously with the samples and used to align the energy. The software Bessy_47b and SimXLite, both developed by the beam scientists at the KMC-3 beamline (BESSY II – Berlin), were used for data processing and extended X-ray absorption fine structure (EXAFS) fitting, respectively. The ranges used for the EXAFS fit were: $k = [2.0; 13.0]$ Å^{-1} and $R = [1.0; 3.5]$ Å for Pt L_3-edge, and $k = [4.0; 12.0]$ Å^{-1} and $R = [1.0; 3.0]$ Å for Co K-edge. The metallic foils were used to determine the amplitude factor, S_0^2, that was equal to 0.967 and 0.805 for the Pt L_3-edge and Co K-edge, respectively. The scattering paths were obtained using the FEFF8 software.

3. Results and discussion

Within this study, 144 h-long single cell experiments were performed. This duration was chosen to exceed the expected break-in period (a duration till the stabilisation of the performance after cell start-up) and thus to investigate the catalyst performance after the initial stabilisation of the FC operation. To assess catalyst activity for both electrode reactions, a series of experiments with various catalysts on individual GDEs were performed, starting with the use of experimental PtCo catalysts on a cathode.

3.1. PtCo behaviour on the cathode

Fig. 1A, B and C show the load and power density curves of three single cells (with the standard **Pt/C catalyst applied on the anode** and **various catalysts**, i.e. Pt/C, PtCo/KB, or PtCo/rGO, **on the cathode**) as a function of time.

MEA C demonstrated the most significant activity improvement during the 144 h of experiment and, at the end of it, the performance of MEA C matched that of the other two MEAs with PtCo-based catalyst on the cathode. On the other hand, both PtCo-based MEAs (KBc and rGOc) reached relatively high performance already during the break-in procedure with only minor further improvements upon consequent 72 h operation. This shows that the full activation of the PtCo catalysts was considerably faster than that of a conventional Pt catalyst. As MEA KBc achieved the highest performance output right after the break-in, its performance remained almost constant and was, by the end of the experiment, slightly surpassed by MEA rGOc in the high current density region. In the low current density region, both PtCo MEAs exhibited identical performance. Based on *IR*-compensated load curves (see Fig. S5 in SI), Tafel analysis (see Fig. S6 in SI) was performed to observe the changes in the activation part of the dynamic load curves during operation (Table 3). In this work, the Tafel equation in the form of $E = E_{\log j=0} + b\log|j|$ was used, where $E_{\log j=0}$ is the potential when $\log|j| = 0$ and holds the information about the inherent rate of an electrochemical reaction. The Tafel slope, b, represents a measure of how electrode potential (or, in this case, voltage) changes with current density and follows the equation $b = -2.303RT/\alpha_{\text{apparent}}F$. Throughout the whole experiment, MEA C showed a lower Tafel slope than MEAs KBc and rGOc, possibly indicating a different rate-determining step.

The EIS spectra are shown in Fig. 1D, E and F, and the resulting values of the respective types of resistance, obtained via EIS fitting on an equivalent circuit, consisting of Ohmic resistance R_Ω and three time constants with corresponding resistances representing charge transfer resistance of the anode $R_{CT,A}$, the cathode $R_{CT,C}$ and mass transport resistance R_{MT} (Fig. S1 in SI), are shown in Fig. 1G, H, and I. In comparison to MEA C, MEA KBc is most active at the beginning and only improves slightly over time, while MEA C undergoes the most pronounced activation. This difference probably results from the presence of Co in MEA KBc and the partial chemical or electrochemical dissolution of the Pt overlayer [33] or dealloying of the Co from the PtCo core connected with Co diffusion towards nanoparticle surface. As Co dissolves during the activation period due to dissolution of uppermost Pt atomic layers, surface defects on nanoparticles, and thus also the ORR activity, are significantly increased, and the performance reaches maximum after 24 h of MEA KBc operation. However, the higher activity of MEA KBc at the start can also stem from the considerably higher porosity of KB, both in the micro- and mesoporous regions [34], which is thus easier for H_3PO_4 to permeate. Consequently, a higher number of active sites is available earlier from the start, which leads to a lower activation resistance at the cathode ($R_{CT,C}$). Both of these effects seem to apply since current in the activation part of the load curves (at high voltages) of MEAs KBc and rGOc increases over time. Meanwhile, MEA KBc reaches overall higher current densities than MEA C in the beginning due to easier H_3PO_4 permeation in the pores. As for the difference between MEA rGOc and KBc, rGO is more hydrophobic, therefore H_3PO_4 permeation in the cathode catalyst layer (CL) can be slower, so the catalyst seemed less active during the first characterisation. Nonetheless, $R_{CT,C}$ gradually decreases in all three cases as H_3PO_4 floods the electrodes and NPs deeper in the CL become activated. This aligns well with other studies found in the literature that have reported the connection between falling R_{CT}, increasing power, and H_3PO_4 redistribution during break-in [35,36]. Lower $R_{CT,C}$ values of the PtCo catalysts at the beginning can also result from a higher intrinsic catalytic activity due to the use of a 3d transition metal. Bevilacqua *et al.* [37] obtained similar results with a PtCo catalyst supported on carbon black, where activation occurred within the first 24 h and the performance remained constant until the last measurement after 120 h of operation.

Fig. 1J, K and L show *ECSA* changes over time (compared to the first measurements) measured by means of H_{UPD} and CO stripping. At this point, it is important to mention that in HT-PEMFCs the H_{UPD} region of the CV is hardly visible, see Fig. S7 in SI. Thus, the *ECSA* values determined by H_{UPD} ($ECSA_{HUPD}$) can be thought of more as a complement to the *ECSA* values measured by CO stripping ($ECSA_{CO}$) rather than being standalone reliable results. One can see that all MEAs behave similarly, and the *ECSA* falls throughout the operation, although there are differences between the catalysts. To address them, the different phenomena occurring during operation must be taken into consideration. First, as H_3PO_4 permeates the cathode CLs, NPs further from the membrane are reached and thus new active sites emerge, as discussed in the previous paragraph. At the same time, degradation processes, such as Ostwald ripening and NP agglomeration and detachment, carbon corrosion, and catalyst poisoning by phosphate anions, continue to occur. The degradation processes and poisoning then result in a gradual *ECSA* decrease. Activation due to H_3PO_4 redistribution stabilises the ECSA to some extent, although the gradual degradation is, at least in the original stage of 144 h long experiment, faster than activation. A similar phenomenon, i.e. increasing HT-PEMFC power with decreasing *ECSA*, was observed by Liu *et al.* [38], who reported increasing power with increasing catalyst

Table 3
$E_{\log j=0}$ (a) and Tafel slopes (b) evaluated from *IR*-compensated load curves of single cells with MEAs containing novel catalysts on the cathodes and Pt/C on the anodes. R^2 stands for the coefficient of determination of the linear fit.

MEA	$a_{24\ h}$ V	$b_{24\ h}$ V dec^{-1}	R^2	$a_{72\ h}$ V	$b_{72\ h}$ V dec^{-1}	R^2	$a_{144\ h}$ V	$b_{144\ h}$ V dec^{-1}	R^2
MEA KBc	0.570	−0.127	0.99	0.601	−0.127	0.99	0.608	−0.129	0.99
MEA rGOc	0.551	−0.108	0.96	0.580	−0.121	0.98	0.599	−0.118	0.98
MEA C	0.582	−0.097	0.98	0.597	−0.088	0.98	0.591	−0.092	0.99

particle sizes in HT-PEMFCs. Finally, both CO and H can displace the adsorbed anions to some degree [39,40]. However, protons have easier access to Pt than CO due to being an inherent part of H_3PO_4, while CO has to diffuse through pores; therefore, $ECSA_{HUPD}$ can be more stable than $ECSA_{CO}$, as is the case in Fig. 1L. Comparing the *ECSA* values for individual MEA cathodes (Fig. 1J, K and L) clearly shows that both PtCo catalysts exhibited higher ECSA and better ECSA retainment than Pt/C. The reason behind the higher ECSA may be the smaller size of PtCo crystallites; however, that would not explain the apparent slower rate of the ECSA decay in the case of the PtCo catalysts. In transition-metal-alloyed catalysts, one must also consider the dissolution of the less noble metal (such as Co) during operation. This dissolution, albeit leading to Co loss, can also provide more active sites on catalyst NP surface due to a rougher surface structure, and counterbalance inherent ECSA loss. This way, more Pt surface can emerge which was also suggested by Shroti and Daletou [11]. They also reported that PtCo alloy catalysts were more resistant to phosphate adsorption, which would explain the generally higher $ECSA_{HUPD}$ values for PtCo catalysts measured in this work, compared to Pt/C. It is worth mentioning that the aforementioned Co dissolution and surface changes happen due to high temperatures and H_3PO_4 concentration in HT-PEMFCs despite the previous *ex situ* activation of the PtCo catalysts by the manufacturer (Section 2.4) PtCo catalysts thus seem to be generally more stable when it comes to ECSA retainment.

The entire MEA was analysed post-mortem by XRD. Components analysed included the anode, cathode, and membrane with adhering CLs, analysed from both sides (see scheme in Fig. S3 in SI). These data were compared with pristine components, providing an overview of changes after FC operation (Fig. 2). An excerpt of a typical X-ray diffractogram of a Pt/C GDE, visible in Fig. 2, exhibits considerable narrowing of Pt reflections around 40°, signalling growth on Pt(111) facets [41]. Data obtained from this measurement were used throughout this section for comparison with other experiments.

The most important feature in the X-ray diffractograms is the position of reflection maxima with respect to the specific reflections of Pt and Co. The signal corresponding to the Pt(111) facet is located at around 40°, followed by another characteristic reflection, corresponding to the Pt(200) facet, around 46°, as can be deduced from diffractograms of the pristine Pt/C GDE (Fig. 2A). In the case of the pristine PtCo GDEs, these characteristic reflection maxima are shifted by approximately 1° to higher values (compared to Pt/C). Therefore, it can be assumed that the position of the reflection maximum at higher angles is related to the increased presence of alloyed Co. As visible in the X-ray patterns of MEA components after operation (Fig. 2B and D), the above-mentioned reflections of PtCo shift towards values typical for Pt, i.e. 40 and 46° This suggests a significant reduction of the Co content on the cathode, i.e. dissolution of Co from alloyed NPs of the cathode PtCo catalysts. On the other hand, Co still seems to be present in alloyed form, since the reflection within the Bragg angle range of 38 to 42° of neither the cathode nor the cathode side of the membrane fully corresponds to the Pt(111) angle 40° and is shifted to higher angles instead. On the anode side, Co seems to have appeared on the membrane. However, metallic Co is not stable under given conditions and alloying of dissolved Co with Pt on the anode is highly improbable. Consequently, as XRD analysis cannot distinguish between two sides of the thin membrane, it is likely that this is an artefact due to traces of the PtCo catalyst being present on

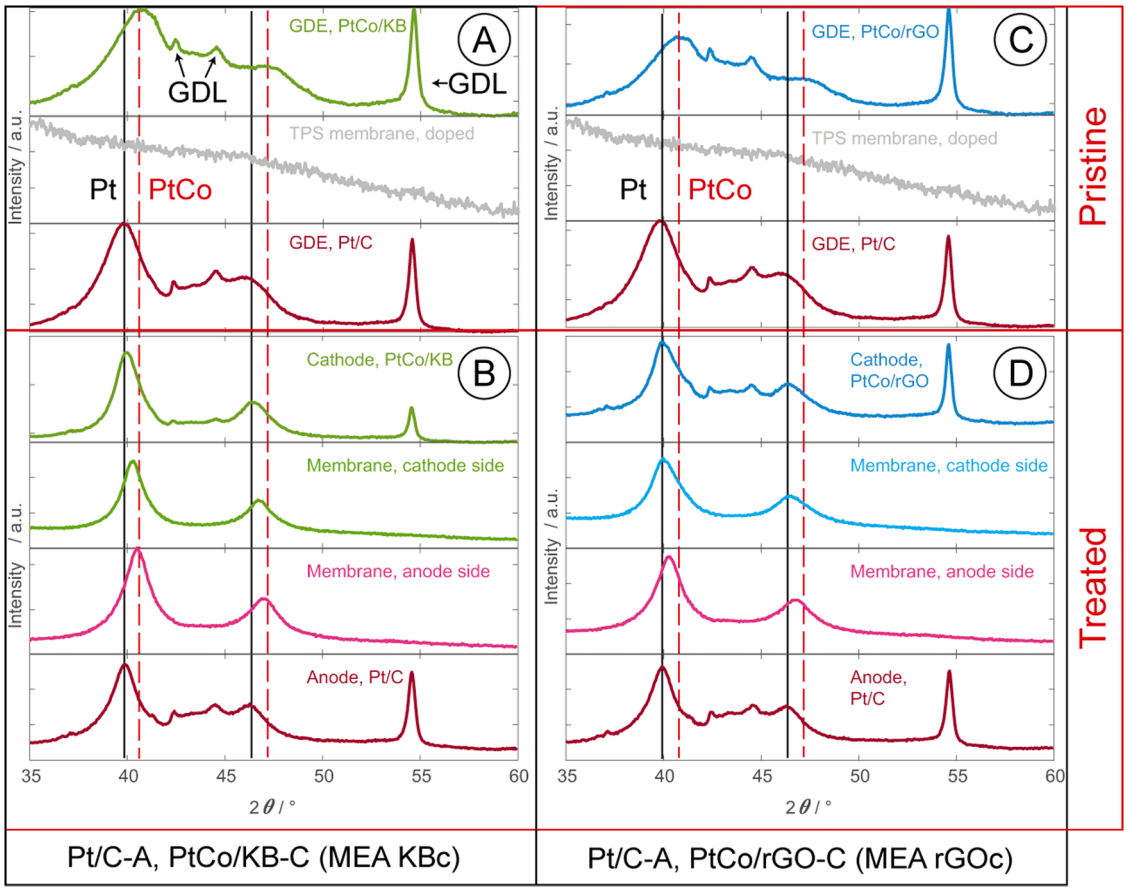

Fig. 2. An excerpt of X-ray diffractograms of MEA KBc (A, B) and rGOc (C, D) with the Pt/C catalyst on the anode and an experimental catalyst on the cathode before (A, C) and after (B, D) the single cell experiments. The vertical lines show the positions of the (111) and (200) reflections of pure Pt (black, full) and the PtCo alloys (red, dashed). The GDL-described arrows point at the reflections for which the presence of the GDL is responsible, i.e. the background of electrode diffractograms, the diffractogram of the GDL is shown in Fig. S4 in SI.

the cathode side of the membrane. The reflections at about 40° in the samples after use are considerably narrower, signalling NP growth. The average diameter of crystallites determined (based on the Pt(111) facet) from the X-ray diffractograms is listed in Table 4.

Results show that the average crystallite dimensions of pristine catalysts are comparable regardless of their composition. However, after operation, MEA C exhibits the largest crystallite size increase, likely as a result of Ostwald ripening of Pt nanoparticles. In the case of MEAs rGOc and KBc, the size increase was not as pronounced. The reason for this behaviour can be likely attributed to several phenomena, partly the presence of Co in the NPs of the alloyed catalysts, which changes the atomic distances on the NP surface (Tables S1–S5 in SI) and the surface energy. These effects make any redeposition of Pt ions more difficult due to lattice mismatch and lower Pt binding energy [42]. Therefore, the alloyed NP growth rate would be significantly slowed down in the experiment stage when the Co content in the subsurface layer is still high. Based on the *ECSA* results in Fig. 1 and XRD results in Table 4, change of ECSA of the pristine and degraded catalyst was estimated (see Tables S6 and S7 in SI). The decrease of ECSA on cathodes was in the following order: PtCo/rGO (22 %) < PtCo/KB (24 %) < Pt/C (40 %). This represents an additional indication of superior stability of PtCo-based catalysts in comparison with Pt/C.

All MEAs used in these experiments were also examined post-mortem by XRF, the results are provided in Table 5 in the form of a m_{Pt}/m_{Co} ratio. The results confirm that, regardless of catalyst support, dissolved Co was transported through the membrane towards the anode.

Table 5 shows that already the pristine GDEs differ in the Co content, which is expected since PtCo/KB contains 1.9 wt.% of Co whereas PtCo/rGO contains 3 wt.% of Co. The mass ratio of Pt:Co in the cathode catalyst after use decreased from 13.1 to 11.6 (i.e. by 11.5 %) and from 7.9 to 7.5 (i.e. by 5.4 %) for PtCo/KB and PtCo/rGO, respectively. Such decrease clearly shows higher Co content in the electrode after use. This can suggest that majority of dealloyed Co remained in the electrode, though not in alloyed/metallic state, while Pt dissolved and was transported to the membrane and/or anode. The proposed transport is also indicated by the small NP dimensions according to XRD (Table 4). Furthermore, since Co dissolves much faster than Pt, the mass ratios mostly reflect the changes of Co content in the CLs. It is important to stress that Co dissolution is feasible only if surface Pt layer is partially dissolved, i.e. the Co and Pt dissolution are simultaneous processes. A direct relation between the amount of dissolved Pt and Co was already demonstrated in case of LT-PEMFCs [43,44] and it can be suggested that this mechanism also acts in HT-PEMFCs. Therefore, it seems that Co in the PtCo/rGO is more stabilised than in the PtCo/KB, as the mass ratio in the former was changed less after the 144 h of single cell operation. The apparent higher amounts of Co on the anode in the case of MEA rGOc can partially be a result of the higher loading of Co in the rGO-supported catalyst. However, as the membranes (after MEA disassembly) hold the majority of the anode CLs, it is probably more precise to deduce the Pt:Co ratios from the CLs adhering to the membrane, not the anodes themselves. That way, the ratios correspond to the initial loading of Co, i.e. there seems to be about 1.5 times more Co at the MEA rGOc anode than at the KBc one.

In the following step, the individual components of the pristine and used MEAs were analysed post-mortem by X-ray absorption near edge structure (XANES) spectroscopy. The original plots of normalised intensity as a function of absorption energy can be found in Fig. S8–10 in SI. Fig. 3A shows the L_3-edge white line (WL), the high and steep absorption peak in the near-edge region, intensities of Pt in MEAs C, KBc and rGOc. In all cases, a modest reduction of the white-line intensity in the post-mortem samples (in comparison with the pristine sample) is visible. This indicates that Pt atoms in the used samples are present in a more reduced (metallic) state. The effect is slightly more pronounced on the cathode, less on the membrane, and the least on the anode. The reason behind that is the growth of the cathode NPs, because of which the ratio between NP surface and volume decreases. Less and less Pt atoms are thus present on the NP surface, where they can get oxidised. As for the membrane, a part of the signal comes from the anode part where NPs are smaller, thus with higher surface-to-volume ratio.

Fig. 3B shows significant changes observed in the WL intensities of MEAs KBc and rGOc at the Co K-edge. A clear increase in the Co WL intensity shows the increasing oxidation state of Co in the system. This supports the previously discussed observation that Co, originally present in the metallic form in the catalyst nanoparticles, oxidises and leaches out towards other parts of the MEA during the FC operation. Furthermore, Co atoms show the highest oxidation state at the anode, followed by those at/in the membrane and finally those at the cathode. The high oxidation state of Co at the anode, where no Co was initially present, is a result of Co being present there only in the form of ions. Conversely, Co is already present from the start of the experiment on the cathode. Since most of it dissolved, there is a visible change but not as pronounced as expected. It is important to mention that XAS is a bulk measurement; therefore, the changes observed in the oxidation state are a result of all species present in the electrode or membrane.

The EXAFS results are presented in the form of coordination numbers $N_{X\text{-}Y}$ (Fig. S11 and S12 in SI), where N represents the number of atoms Y (Co, Pt, O) around the central atom of X (Pt or Co). The fit parameters, including the coordination numbers for Fig. S11 and S12, are summarised in Tables S1–S5, the experimental and fit data are shown in Fig. S13–S17 in SI.

Pt L_3-edge (Fig. S11 in SI): For MEA C samples (anode, membrane, cathode) in Fig. S11A and B, there is an increase in $N_{Pt\text{-}Pt}$ compared to the pristine Pt/C, reaching its highest value of 8.7 at the cathode. This agrees well with the increase in the Pt crystallite size discussed above. $N_{Pt\text{-}O}$ decreases significantly at the anode and membrane. The corresponding values on the cathode could not be determined due to low signal intensity.

For the PtCo/KB and PtCo/rGO samples (Fig. S11C–H in SI), $N_{Pt\text{-}Co}$ reaches the highest value for pristine samples. Moreover, except for pristine samples, it was impossible to establish $N_{Pt\text{-}Co}$ values for MEAs KBc and rGOc, indicating Co leaching from the NPs. However, the $N_{Pt\text{-}Co}$-related errors were, in some cases, as high as 200 % of the fitted values, so a more detailed discussion is not meaningful. $N_{Pt\text{-}Pt}$ increases for all samples, with the most dramatic increase observed for the cathodes, which results from NP growth being the most pronounced there. Similarly, $N_{P\text{-}O}$ mostly decreases on cathodes as the ratio of surface to volume also decreases.

The EXAFS fits for the **Co K-edge** were only possible for samples with an adequate signal-to-noise ratio (Fig. S12 in SI). Samples where the presence of Co was only detectable are shown without a bar in the plots

Table 4
Dimensions of Pt crystallites in the direction perpendicular to the Pt(111) facet of pristine GDEs and parts of MEAs used in the experiments with PtCo catalysts on cathodes (MEA KBc and rGOc), Pt/C (MEA C) for comparison.

Cathode catalyst in MEA	Pristine GDE	Anode	Membrane anode	Cathode	Membrane cathode
PtCo/KB; sizes / nm	4.5	7.3	5.5	6.1	6.1
PtCo/rGO; sizes / nm	5.4	7.4	5.4	7.2	5.1
Pt/C; sizes / nm	5.3	9.7	5.6	10.3	8.4

Table 5
Mass ratios of Pt to Co (m_{Pt}/m_{Co}) on electrodes and the respective sides of the membranes from MEAs used in experiments with novel catalysts on cathodes and Pt/C on anodes (MEA KBc and rGOc).

Sample	PtCo/KB			PtCo/rGO		
	Pristine GDE	Cathode	Anode	Pristine GDE	Cathode	Anode
Electrodes	13.1	11.6	31.4	7.9	7.5	15.3
Membranes	–	34.7	61.9	–	23.5	40.0

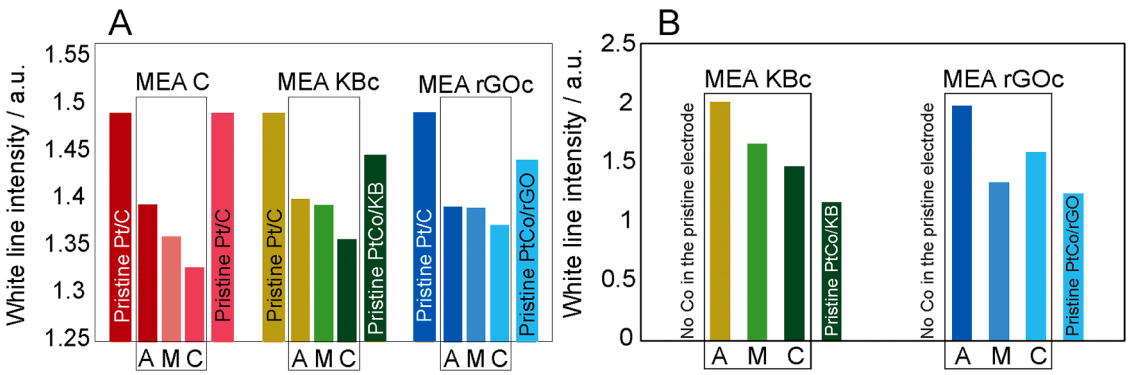

Fig. 3. White line intensities for MEAs C, KBc and rGOc at the Pt L_3-edge (A) and at the Co K-edge (B). The MEAs themselves are bordered by a rectangle, next to which bars of pristine materials are shown. A, M, and C represent the anode, membrane, and cathode, respectively. Since the Co K-edge was not measured for pristine Pt/C, no pristine material bar can be found next to the anodes in B.

in Fig. S12. Generally, due to the low amount of Co in the samples (see Tables S4 and S5 in SI), the error associated with Co K-edge fits is considerably higher than that of the Pt L_3-edge.

For all catalysts, $N_{\text{Co-Pt}}$ decreases considerably in all components, especially at the cathodes, indicating that Co atoms mostly leached out from the NP structure, although part of Co seems to remain in the alloy as the values of $N_{\text{Co-Pt}}$ and $N_{\text{Co-Co}}$ are non-zero. $N_{\text{Co-O}}$ increases for all samples, suggesting that Co atoms are mostly bound with O (possibly as Co phosphates). Notably, at the cathodes of all rGO MEAs, $N_{\text{Co-O}}$ shows the highest values (3.6, 6.0 and 5.7 for MEA rGOc, rGOa and rGOb, respectively).

3.2. *Effect of PtCo used on the anode*

To examine the lifecycle of Co in the MEA and the performance of PtCo alloys for hydrogen oxidation reaction, the PtCo catalysts were tested also on the anode side of the cell. In all cases, Pt/C was used as the cathode catalyst. Fig. 4A–C show the load and power density curves in the same manner as in Section 3.1.

In these experiments, both PtCo catalysts on the anode show significantly worse performance than Pt/C after the break-in procedure. Moreover, while MEA rGOa is stable in its performance, MEA KBa loses activity (peak power density decreased by about 32 % between the first and the last characterisation). This can be directly related to the limited stability of the PtCo alloy. In particular, it seems that Co, gradually dissolving from NPs most likely precipitates in the form of phosphates at/near the NPs in the CL. Therefore, it physically blocks a part of the active sites and could significantly impede proton and/or H_2 transport. Co could also stay at least partially in the alloy. These effects will be discussed in more detail later in this section together with the XRF and XAS results. Concerning the Tafel slope parameters presented in Table 6, obtained from the *iR*-compensated load curves (see Fig. S5 and S6 in SI), they gradually change in MEAs rGOa and KBa. The decrease in $E_{\log j=0}$ during operation could be connected to blocking of active sites, most likely by Co phosphates. Interestingly, *b* grows towards more negative values that, by the end of the experiment, resemble the *b* values for the MEAs KBc and rGOc (Table 3), possibly resulting from the stabilisation of PtCo NPs after partial Co dissolution.

The EIS spectra of MEAs KBa and rGOa, presented in Fig. 4D–F, provide further insight into performance changes during FC operation. EIS spectra confirm the previous observation that the performance of MEA rGOa remains roughly constant. On the other hand, MEA KBa shows a very high polarisation/mass transfer resistance that grows over time, causing the performance to deteriorate. Three half-circles are visible in the corresponding impedance spectra upon careful analysis. The high frequency polarisation resistance corresponds to the kinetically fast HOR, and since the cathode uses Pt/C, the half-circle in the mid-frequency-range most probably corresponds to the slower ORR. The half-circle at low frequency values would then correspond to the slowest process – mass transport limitations (R_{MT}), which is very pronounced in the case of MEA KBa. Since the chemical structure and features of KB and Vulcan XC-72, used for HiSPEC 4000, do not differ significantly except for higher intrinsic porosity of KB, especially in mesopores [34], it is likely the presence of Co phosphates that impedes proton transport and/or H_2 transport to the active sites, as implied earlier. This, in turn, would explain the mass transport resistance measured by EIS. As for the main reason for the poor performance of MEAs KBa and rGOa, one could argue that already the presence of the PtCo alloys on the anode is enough to impede the HOR kinetics. However, such an effect would be visible in the low current density part of the load curves in Fig. 4, which is not the case. On the contrary, MEAs KBa and rGOa show marks of impeded mass transport in the load curves and EIS.

Cathode (Pt/C) *ECSA* values are shown in Fig. 4J–L. The values of $ECSA_{\text{CO}}$ are very similar for all MEAs regardless of the anode catalyst. The $ECSA_{\text{HUPD}}$ values, on the other hand, seem to be affected by the anode catalyst. A possible reason lies in the fact that the anode is used as a pseudo-reference electrode. Therefore, any changes resulting in anode potential shift, including the presence of Co and its subsequent partial dissolution, affect actual cathode potentials on the standard hydrogen scale. Since the voltage scans for H_{UPD} are determined within fixed cell voltage limits, those may not ideally reflect the H_{UPD}. A change in measured voltage could alter the calculated value of $ECSA_{\text{HUPD}}$.

When the PtCo catalysts were used on the cathode, almost no alloyed Co was found there by XRD after 144 h of operation. Similarly, the comparison of the X-ray patterns of the anodes with PtCo catalysts suggests some Co dissolution and dealloying. This is documented by the (111) and (200) reflection position shift to lower angle values in Fig. 5B and D, albeit less pronounced than in the case of the PtCo cathodes. In particular, XRD of anodes of both the MEA KBa and rGOa show a lower shift towards pure Pt, implying the presence of alloyed Co even after HT-PEMFC operation. XRD analysis of the anode side of the membranes provides similar results with slightly more pronounced Pt reflections convoluted with the Co ones. Despite the anode potentials being rather low (0–200 mV), the PtCo alloy does not seem to be stable when in contact with hot and concentrated H_3PO_4, unless covered by overlayers (shell) of Pt [45].

Changes in catalyst crystallite sizes in MEAs were estimated on the basis of X-ray diffractograms, and the results are presented in Table 7. The PtCo crystallite size growth on the anode was observed only for MEA rGOa. Since the majority of the CL adhered to the membrane, the crystallite sizes could not be determined directly from the anode. The growth of Pt crystallites (of Pt/C) on the cathode was almost independent of the type of catalyst present on the anode side of MEA, although it was somewhat more pronounced for MEA C, where no Co was present.

The mass ratio of Pt:Co, determined from XRF, was largely unchanged on the anodes and the anode side of the membranes. At the

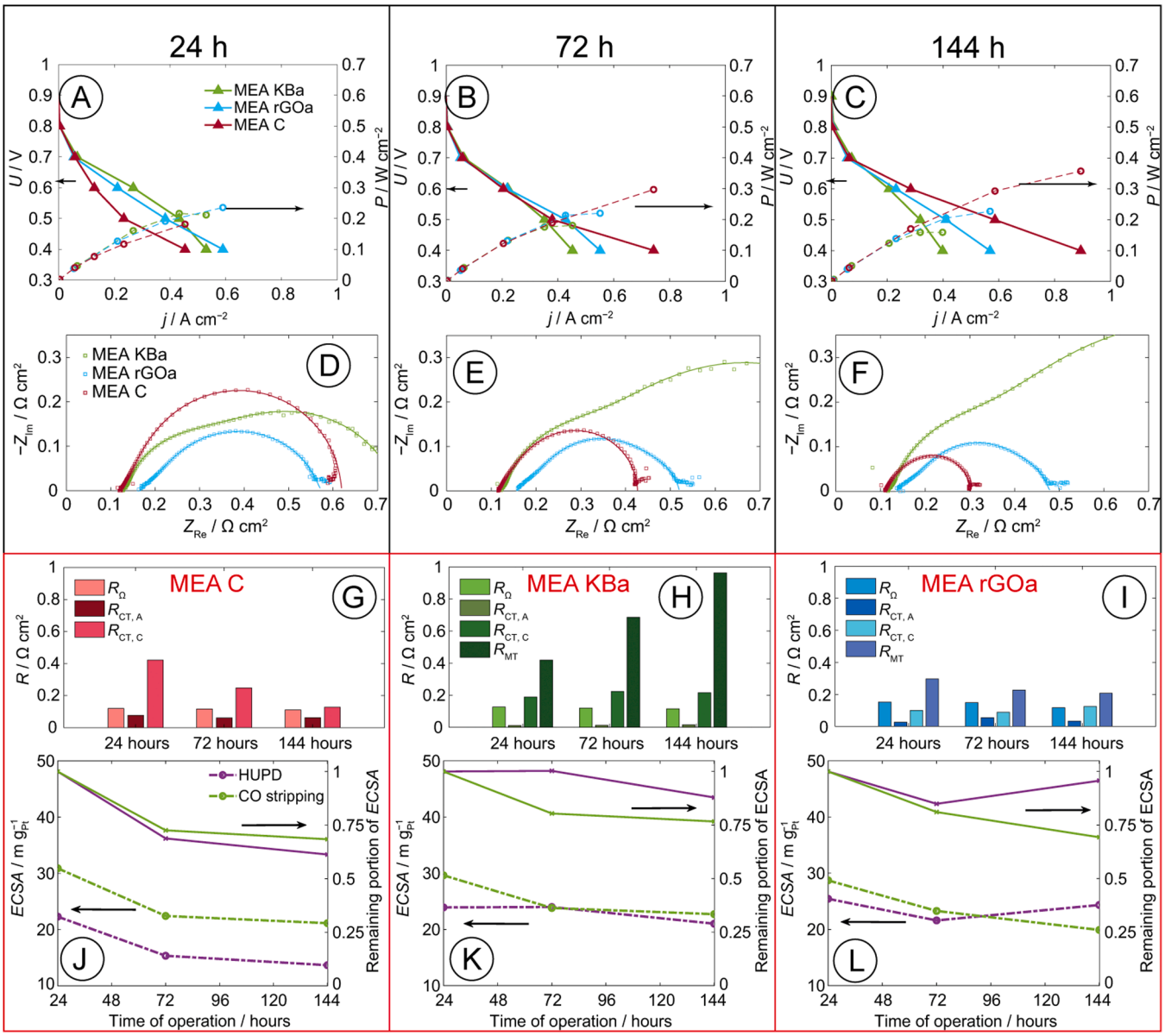

Fig. 4. Results of the testing protocol for MEAs with Pt/C on the cathode and various catalysts on the anode side of the fuel cell, see plot inset. A, B, C – stationary load and power density curves measured after 24, 72, and 144 h of operation, respectively; D, E, F – corresponding impedance spectra recorded at a voltage of 0.5 V, voltage amplitude was 10 mV, MEA C with Pt/C for comparison; G, H, I – bar graphs of the resistance of MEAs obtained with EIS spectra fitting; J, K, L – *ECSA* (dash-dotted lines) and the respective remaining portions of *ECSA* relating to the first measurement (thinner, dashed lines) obtained using H_{UPD} and CO stripping analyses. R_Ω is the ohmic resistance, $R_{CT,A}$ and $R_{CT,C}$ are the charge transfer resistances of the anode and cathode, respectively, R_{MT} is the mass transport resistance. In these graphs, KBa symbolises the MEA with PtCo/KB on the anode, rGOa stands for the MEA with PtCo/rGO on the anode and MEA C stands for Pt/C on the anode. All three MEAs utilise Pt/C on the cathode. More information can be found in Table 2.

Table 6
$E_{\log j=0}$ (*a*) and Tafel slopes (*b*) evaluated from *IR*-compensated load curves of single cells with MEAs containing novel catalysts on the anodes and Pt/C on the cathodes. R^2 stands for the coefficient of determination of the linear fit.

MEA	$a_{24\ h}$ V	$b_{24\ h}$ V dec^{-1}	R^2	$a_{72\ h}$ V	$b_{72\ h}$ V dec^{-1}	R^2	$a_{144\ h}$ V	$b_{144\ h}$ V dec^{-1}	R^2
MEA KBa	0.604	−0.089	0.98	0.589	−0.099	0.98	0.572	−0.122	0.98
MEA rGOa	0.580	−0.093	0.95	0.571	−0.101	0.98	0.554	−0.115	0.97
MEA C	0.582	−0.097	0.98	0.597	−0.088	0.98	0.591	−0.092	0.99

same time, small amounts of Co were detected on the cathodes, as documented in Table 8. Compared to the PtCo catalysts' use on the cathodes, the values here are similar, which suggests that regardless of the polarisation, there is always some transport of dissolved Co from one electrode to the other. Since Co is present in both alloyed and dissolved form, it seems even more plausible that the worse performance of MEAs KBa and rGOa (in comparison with MEAs KBc and rGOc) is a result of the poorer catalytic properties of PtCo alloys towards the HOR [46] and

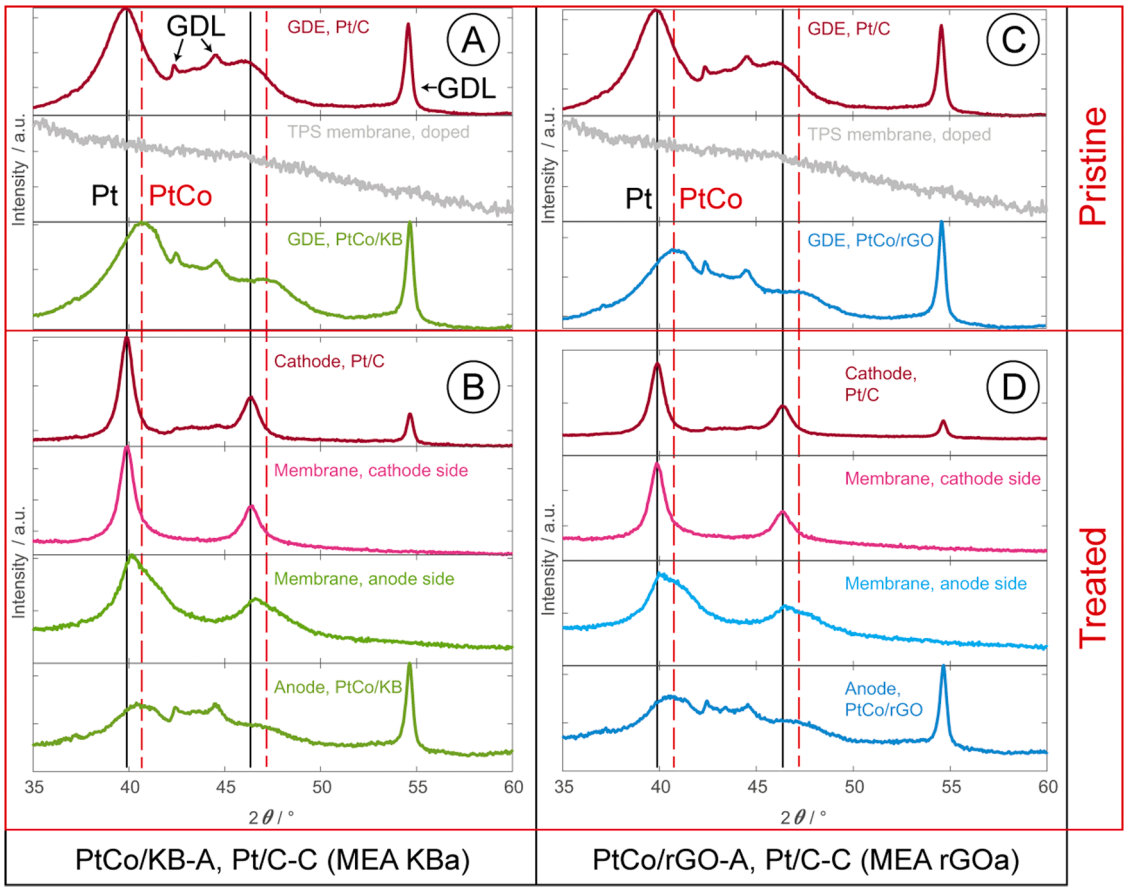

Fig. 5. A subset of X-ray diffractograms of MEA KBa (A, B) and rGOa (C, D) with the Pt/C catalyst on the cathode and an experimental catalyst on the anode before (A, C) and after (B, D) the single cell experiments. The vertical lines show the positions of the (111) and (200) reflections of pure Pt (black, full) and the PtCo alloys (red, dashed) The GDL-described arrows point at the reflections for which the presence of the GDL is responsible, i.e. the background of electrode diffractograms, the diffractogram of the GDL is shown in Fig. S4 in SI.

Table 7
Dimensions of Pt crystallites in the direction perpendicular to the Pt(111) facet of pristine GDEs and parts of MEAs used in the experiments with PtCo catalysts on anodes (MEA KBa and rGOa), Pt/C (MEA C) for comparison.

Anode catalyst in MEA	Pristine GDE	Anode	Membrane anode	Cathode	Membrane cathode
PtCo/KB; size/nm	4.5	–	4.2	9.8	7.8
PtCo/rGO; size/nm	5.4	–	7.3	9.5	7.9
Pt/C; size/nm	5.3	9.7	5.6	10.3	8.4

mass transport losses due to Co phosphate formation. The CL contains about 10 wt.% of PBI as a binder, and each repeating unit is protonated by at least two molecules of H_3PO_4 [47]. Considering this and the catalyst loading, it is possible to calculate the molar ratio of Co:H_3PO_4 in the CL, which is 7.1 for PtCo/rGO and 4.5 for PtCo/KB. These ratios suggest that, when dissolved, Co can poison the binder quite effectively by forming phosphates that impede mass transport. Nonetheless, even if all Co dissolves, not all H_3PO_4 will necessarily be bound to it, as there is also free H_3PO_4 in the CL. Still, a significant part of the H_3PO_4 in the CL binder (in the vicinity of the catalyst particles) can be bound in the form of Co phosphates. At this point, a question could (and should) be raised as to why this effect does not occur in the same way at the cathode, the more so since the Co present there dissolves faster than on the anode. However, unlike at the anode, water is produced at the cathode and brought to the gas diffusion electrode bulk by electroosmotic drag. As a result, the H_3PO_4 concentration at the cathode is likely lower, which together with migration can help the acid spread deeper into the CL, removing a portion of dissolved Co and reducing binder poisoning at the cathode.

Table 8
Mass ratios of Pt to Co (m_{Pt}/m_{Co}) on electrodes and the respective sides of the membranes from MEAs used in experiments with novel catalysts on anodes and Pt/C on cathodes (MEA KBa and rGOa).

Sample	PtCo/KB			PtCo/rGO		
	Pristine GDE	Cathode	Anode	Pristine GDE	Cathode	Anode
Electrodes	13.1	65.0	11.4	7.9	34.5	8.0
Membranes	–	31.1	20.2	–	18.7	10.7

Fig. 6A and B show the WL intensities of MEAs KBa and rGOa at the Pt L_3-edge (A) and Co K-edge (B). Regarding the Pt L_3-edge, the trends are similar to MEAs KBc and rGOc – the WL intensity decreases after operation, mostly for cathodes where the NPs grow the most. For both MEAs, barely any changes are visible in Fig. 6B on the anode and membrane due to the fact that there is still some Co in the alloy. However, at the cathode, Co is present only in the ionic form, therefore the WL intensity is high. It was suggested that the leached Co is present in the MEA in the form of phosphates. However, no such species could be detected by XRD (while being visible by XAS). This may be explained in two different ways: either the Co phosphate is amorphous (as the XRD results suggest, see Fig. S18 in SI) or it does not precipitate.

In Fig. S11 in SI, XAS results of electrode and membrane samples are summarised. In this case, the error is maximally up to 50 %. $N_{Pt\text{-}Co}$ shows that there is some Co present in the alloy in the anode and membrane in

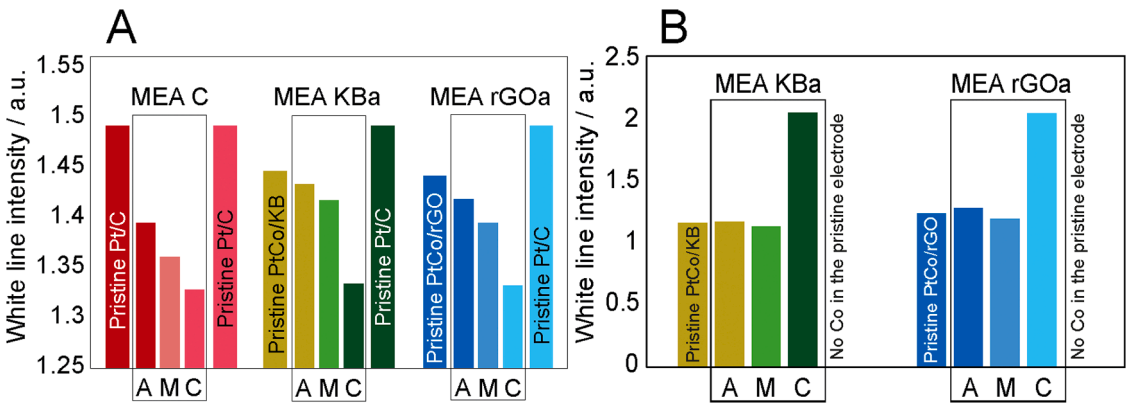

Fig. 6. White line intensities for MEAs C, KBa and rGOa at the Pt L_3-edge (A) and at the Co K-edge (B). The MEAs themselves are bordered by a rectangle, next to which bars of pristine materials are shown. A, M, and C represent the anode, membrane, and cathode, respectively. Since the Co K-edge was not measured for pristine Pt/C, no pristine material bar can be found next to the cathodes in B.

MEAs KBa and rGOa. In both cases, $N_{Pt\text{-}Pt}$ increases in all components, especially in the cathode, where the NPs grow the most due to the oxidising environment. $N_{Pt\text{-}O}$, on the other hand, is the opposite and decreases. Regarding the Co K-edge (Fig. S12 in SI), $N_{Co\text{-}Co}$ and $N_{Co\text{-}Pt}$ were only obtainable for the components where Co stayed in the alloy, i.e. the anode and membrane. On the anode, $N_{Co\text{-}Co}$ and $N_{Co\text{-}Pt}$ are generally very similar to the pristine values, as the dissolution is quite low and most likely limited to a shallow subsurface layer. As for $N_{Co\text{-}O}$, in MEA KBa, results were only obtainable for the anode and membrane, whereas in MEA rGOa, $N_{Co\text{-}O}$ was the highest in the cathode.

To complement the previous experiments performed with PtCo catalysts on the cathode and anode, and compare the resulting impact of Co on performance, the PtCo catalysts were used on both electrodes. The resulting effect was similar to the one on the anode where the overall performance was impeded because of mass transport hindered by Co phosphates formed. However, improved performance of the cathode compensated, to a certain degree, the negative impact of Co on the anode. This confirmed that Co is transported across the MEA and significantly impacts electrode reactions. The results of the experiments with PtCo catalysts on both electrodes are shown in Fig. S19 in SI and further discussed in Section S10 in SI.

4. Conclusion

In this study, the potential of PtCo intermetallic alloys as alternative HT-PEMFC catalysts was investigated. The observed partial dealloying of Co leads to stabilisation of the Pt nanoparticle surface, facilitating active sites for the ORR and delaying the degradation caused by Ostwald ripening. When used on the cathode, both PtCo catalysts with either Ketjenblack or reduced graphene oxide support showed stable power performance comparable to that of the Pt/C catalyst. Unlike the commercial Pt/C material, PtCo catalysts exhibited more stable ECSA, probably due to processes such as partial dissolution of Co and the gradual carbon support pore opening. On the other hand, the use of PtCo catalysts on the anode or on both electrodes was accompanied by severe mass transport limitations, probably due to the formation of Co phosphates in the CL. The impact of Co dealloying on the anode was lower for PtCo/rGO than for PtCo/KB, despite a higher Co content in the former. This suggests that the right catalyst support can considerably decrease the potential negative effects of dealloying in HT-PEMFCs. The complex nature of Co transport in MEA was underlined by post-mortem spectroscopic analyses, suggesting the minor transport of Co from the cathode. On the other hand, the majority of Co dissolved at the anode remained in the anode CL. Based on these results, intermetallic PtCo alloy catalysts show promise as an alternative to Pt cathode catalysts in HT-PEMFCs, exhibiting improved activity and stability during short-term single cell operation. However, long-term operation of a cell with a PtCo cathode has to be further verified, especially due to Co dealloying. This can impact the stability of the cathode PtCo catalyst, and activity of the anode due to Co transport from the cathode and consequent Co phosphate formation on the anode.

CRediT authorship contribution statement

V. Domin: Writing – review & editing, Writing – original draft, Visualization, Validation, Resources, Methodology, Investigation, Formal analysis, Data curation, Conceptualization. **M. Prokop:** Writing – review & editing, Writing – original draft, Visualization, Validation, Resources, Methodology, Investigation, Formal analysis, Data curation, Conceptualization. **T. Bystron:** Writing – review & editing, Validation, Supervision, Methodology, Formal analysis, Conceptualization. **M. Gatalo:** Writing – review & editing, Resources, Investigation. **L. Pavko:** Resources, Investigation. **N. Hodnik:** Writing – review & editing, Resources, Funding acquisition. **B.F. Gomes:** Writing – review & editing, Writing – original draft, Visualization, Validation, Resources, Methodology, Investigation, Formal analysis, Data curation, Conceptualization. **C.M.S. Lobo:** Writing – review & editing, Validation, Resources, Investigation, Formal analysis, Data curation. **C.E. Hartwig:** Writing – review & editing, Validation, Resources, Investigation, Formal analysis, Data curation. **C. Roth:** Writing – review & editing, Supervision, Funding acquisition. **M. Paidar:** Supervision, Conceptualization. **K. Bouzek:** Writing – review & editing, Supervision, Project administration, Funding acquisition, Conceptualization.

Declaration of competing interest

The authors declare that they have no known competing financial interests or personal relationships that could have appeared to influence the work reported in this paper.

Acknowledgements

We acknowledge the Czech Science Foundation (GAČR) for its support through the project No. 22-23668 K. The work was also supported from the grants of Specific university research – grant No. A2_FCHT_2024_041 and A2_FCHT_2025_088 of University of Chemistry and Technology, Prague, and by the project "The Energy Conversion and Storage", funded as project No. CZ.02.01.01/00/22_008/0004617 by Programme Johannes Amos Comenius, call Excellent Research. We thank DESY (Hamburg, Germany), a member of the Helmholtz Association, for the provision of experimental facilities. Parts of this research were carried out at PETRA III and we would like to thank Edmund Welter for assistance in using the P65 beamline. Beamtime was allocated for proposal I-20230933. The authors would like to acknowledge the

Slovenian Research and Innovation Agency (ARIS) programs P2-0393 and I0-0003; the projects NC-0016, N2-0257, N2-0385, J7-50227 and J2-60043; European Research Council (ERC) Proof of Concept Grant STABLECAT (grant agreement ID: 966654); NATO Science for Peace and Security Program (Grant G6230); B.F.G and C.R. thank the Federal Ministry of Education and Research (BMBF) for the funding of projects Live XAS (Grant 05K22WC1) and HighHy (Grant 03SF0689B). The authors acknowledge partial support from the Republic of Slovenia, Ministry of Higher Education, Science and Innovation, and from the European Union – NextGenerationEU in the framework of the project HyBReED, that is part of the Slovenian Recovery and Resilience Plan. Views and opinions expressed are however those of the authors only and do not necessarily reflect those of the Republic of Slovenia, Ministry of Higher Education, the European Union or the European Commission. Neither the Republic of Slovenia, Ministry of Higher Education, Science and Innovation, European Union nor the European Commission can be held responsible for them.

Supplementary materials

Supplementary material associated with this article can be found, in the online version, at doi:10.1016/j.electacta.2025.146707.

Data availability

Data will be made available on request.

References

[1] J.S. Yang, L.N. Cleemann, T. Steenberg, C. Terkelsen, Q.F. Li, J.O. Jensen, H. A. Hjuler, N.J. Bjerrum, R.H. He, High molecular weight polybenzimidazole membranes for High temperature PEMFC, Fuel Cells 14 (2014) 7–15, https://doi.org/10.1002/fuce.201300070.

[2] Q. Li, R. He, J.-A Gao, J.O. Jensen, N.J. Bjerrum, The CO poisoning effect in PEMFCs operational at temperatures up to 200°C, J. Electrochem. Soc. 150 (2003) A1599, https://doi.org/10.1149/1.1619984.

[3] S.K. Das, A. Reis, K.J. Berry, Experimental evaluation of CO poisoning on the performance of a high temperature proton exchange membrane fuel cell, J. Power. Sources. 193 (2009) 691–698, https://doi.org/10.1016/j.jpowsour.2009.04.021.

[4] S. Simon Araya, V. Liso, X. Cui, N. Li, J. Zhu, S.L. Sahlin, S.H. Jensen, M.P. Nielsen, S.K. Kær, A review of the methanol economy: the fuel cell route, Energies. (Basel) (2020), https://doi.org/10.3390/en13030596.

[5] M. Prokop, T. Bystron, P. Belsky, O. Tucek, R. Kodym, M. Paidar, K. Bouzek, Degradation kinetics of Pt during high-temperature PEM fuel cell operation part III: voltage-dependent Pt degradation rate in single-cell experiments, Electrochim. Acta 363 (2020) 137165, https://doi.org/10.1016/j.electacta.2020.137165.

[6] B.F. Gomes, M. Prokop, T. Bystron, R. Loukrakpam, J. Melke, C.M.S. Lobo, M. Fink, M. Zhu, E. Voloshina, M. Kutter, H. Hoffmann, K.V. Yusenko, A.G. Buzanich, B. Röder, K. Bouzek, B. Paulus, C. Roth, Following adsorbed intermediates on a platinum gas diffusion electrode in H3PO3-containing electrolytes using In situ X-ray absorption spectroscopy, ACS. Catal. 12 (2022) 11472–11484, https://doi.org/10.1021/acscatal.2c02630.

[7] W. Li, D. Wang, T. Liu, L. Tao, Y. Zhang, Y.C. Huang, S. Du, C.L. Dong, Z. Kong, Y. F. Li, S. Lu, S. Wang, Doping-modulated strain enhancing the phosphate tolerance on PtFe alloys for high-temperature proton exchange membrane fuel cells, Adv. Funct. Mater. 32 (2022) 2109244, https://doi.org/10.1002/adfm.202109244.

[8] H. Park, K.M. Kim, H. Kim, D.K. Kim, Y.S. Won, S.K. Kim, Electrodeposition-fabricated PtCu-alloy cathode catalysts for high-temperature proton exchange membrane fuel cells, Korean J. Chem. Eng. 35 (2018) 1547–1555, https://doi.org/10.1007/s11814-018-0059-z.

[9] X. Zhang, Z. An, Z. Xia, H. Li, X. Xu, S. Yu, S. Wang, G. Sun, Phosphoric acid resistance PtCu/C oxygen reduction reaction electrocatalyst for HT-PEMFCs: a theoretical and experimental study, Appl. Surf. Sci. 619 (2023) 156663, https://doi.org/10.1016/j.apsusc.2023.156663.

[10] P. Long, S. Du, Q. Liu, L. Tao, C. Peng, T. Wang, K. Gu, C. Xie, Y. Zhang, R. Chen, S. Lu, Y. Cheng, W. Feng, S. Wang, Fluorination-enabled interface of PtNi electrocatalysts for high-performance high-temperature proton exchange membrane fuel cells, Sci. China Mater. 65 (2022) 904–912, https://doi.org/10.1007/s40843-021-1839-8.

[11] N. Shroti, M.K. Daletou, The Pt–Co alloying effect on the performance and stability of high temperature PEMFC cathodes, Int. J. Hydrogen. Energy 47 (2022) 16235–16248, https://doi.org/10.1016/j.ijhydene.2022.03.109.

[12] A. Schenk, C. Grimmer, M. Perchthaler, S. Weinberger, B. Pichler, C. Heinzl, C. Scheu, F.-A. Mautner, B. Bitschnau, V. Hacker, Platinum–cobalt catalysts for the oxygen reduction reaction in high temperature proton exchange membrane fuel cells – Long term behavior under ex-situ and in-situ conditions, J. Power. Sources. 266 (2014) 313–322, https://doi.org/10.1016/j.jpowsour.2014.05.023.

[13] Y. Devrim, E.D. Arıca, A. Albostan, Graphene based catalyst supports for high temperature PEM fuel cell application, Int. J. Hydrogen. Energy 43 (2018) 11820–11829, https://doi.org/10.1016/j.ijhydene.2018.03.047.

[14] R. Lin, T. Zheng, L. Chen, H. Wang, X. Cai, Y. Sun, Z. Hao, Anchored Pt-Co nanoparticles on honeycombed graphene as highly durable catalysts for the oxygen reduction reaction, ACS. Appl. Mater. Interfaces. 13 (2021) 34397–34409, https://doi.org/10.1021/acsami.1c08810.

[15] L. Pavko, M. Gatalo, T. Đukić, F. Ruiz-Zepeda, A.K. Surca, M. Šala, N. Maselj, P. Jovanovič, M. Bele, M. Finšgar, B. Genorio, N. Hodnik, M. Gaberšček, Correlating oxygen functionalities and electrochemical durability of carbon supports for electrocatalysts, Carbon. N. Y. 215 (2023) 118458, https://doi.org/10.1016/j.carbon.2023.118458.

[16] X. Wang, W. Li, Z. Chen, M. Waje, Y. Yan, Durability investigation of carbon nanotube as catalyst support for proton exchange membrane fuel cell, J. Power. Sources. 158 (2006) 154–159, https://doi.org/10.1016/j.jpowsour.2005.09.039.

[17] Y. Devrim, E.D. Arıca, Multi-walled carbon nanotubes decorated by platinum catalyst for high temperature PEM fuel cell, Int. J. Hydrogen. Energy 44 (2019) 18951–18966, https://doi.org/10.1016/j.ijhydene.2019.01.051.

[18] Q. Zhang, Y. Ling, W. Cai, X. Yu, Z. Yang, High performance and durability of polymer-coated Pt electrocatalyst supported on oxidized multi-walled in high-temperature polymer electrolyte fuel cells, Int. J. Hydrogen. Energy 42 (2017) 16714–16721, https://doi.org/10.1016/j.ijhydene.2017.05.070.

[19] A. Sarkar, A. Manthiram, Synthesis of Pt@Cu core−shell nanoparticles by galvanic displacement of Cu by Pt4+ ions and their application as electrocatalysts for oxygen reduction reaction in fuel cells, J. Phys. Chem. C 114 (2010) 4725–4732, https://doi.org/10.1021/jp908933r.

[20] K. Sasaki, H. Naohara, Y. Cai, Y.M. Choi, P. Liu, M.B. Vukmirovic, J.X. Wang, R. R. Adzic, Core-protected platinum monolayer shell high-stability electrocatalysts for fuel-cell cathodes, Angewandte Chemie Int. Ed. 49 (2010) 8602–8607, https://doi.org/10.1002/anie.201004287.

[21] M. Gatalo, M. Bele, F. Ruiz-Zepeda, E. Šest, M. Šala, A.R. Kamšek, N. Maselj, T. Galun, P. Jovanovič, N. Hodnik, M. Gaberšček, A double-passivation water-based galvanic displacement method for reproducible gram-scale production of high-performance platinum-alloy electrocatalysts, Angewandte Chemie Int. Ed. 58 (2019) 13266–13270, https://doi.org/10.1002/anie.201903568.

[22] M. Gatalo, F. Ruiz-Zepeda, N. Hodnik, G. Dražić, M. Bele, M. Gaberšček, Insights into thermal annealing of highly-active PtCu3/C oxygen reduction reaction electrocatalyst: an in-situ heating transmission electron microscopy study, Nano Energy 63 (2019) 103892, https://doi.org/10.1016/j.nanoen.2019.103892.

[23] M. Gatalo, L. Moriau, U. Petek, F. Ruiz-Zepeda, M. Šala, M. Grom, T. Galun, P. Jovanovič, A. Pavlišič, M. Bele, N. Hodnik, M. Gaberšček, CO-assisted ex-situ chemical activation of Pt-Cu/C oxygen reduction reaction electrocatalyst, Electrochim. Acta 306 (2019) 377–386, https://doi.org/10.1016/j.electacta.2019.03.153.

[24] M. Gatalo, A.M. Bonastre, L.J. Moriau, H. Burdett, F. Ruiz-Zepeda, E. Hughes, A. Hodgkinson, M. Šala, L. Pavko, M. Bele, N. Hodnik, J. Sharman, M. Gaberšček, Importance of chemical activation and the effect of low operation voltage on the performance of Pt-alloy fuel cell electrocatalysts, ACS. Appl. Energy Mater. 5 (2022) 8862–8877, https://doi.org/10.1021/acsaem.2c01359.

[25] M. Prokop, T. Bystron, M. Paidar, K. Bouzek, H3PO3 electrochemical behaviour on a bulk Pt electrode: adsorption and oxidation kinetics, Electrochim. Acta 212 (2016) 465–472, https://doi.org/10.1016/j.electacta.2016.07.045.

[26] M. Prokop, T. Bystron, K. Bouzek, Electrochemistry of phosphorous and hypophosphorous acid on a Pt electrode, Electrochim. Acta 160 (2015) 214–218, https://doi.org/10.1016/j.electacta.2015.01.097.

[27] L. Pavko, M. Gatalo, M. Finšgar, F. Ruiz-Zepeda, K. Ehelebe, P. Kaiser, M. Geuß, T. Đukić, A.K. Surca, M. Šala, M. Bele, S. Cherevko, B. Genorio, N. Hodnik, M. Gaberšček, Graphene-derived carbon support boosts proton exchange membrane fuel cell catalyst stability, ACS. Catal. 12 (2022) 9540–9548, https://doi.org/10.1021/acscatal.2c01753.

[28] P. Heizmann, H. Nguyễn, M. von Holst, A. Fischbach, M. Kostelec, F. Lopez, M. Bele, L. Pavko, T. Đukić, M. Šala, F. Ruiz-Zepeda, C. Klose, M. Gatalo, N. Hodnik, S. Vierrath, M. Breitwieser, Alternative and facile production pathway towards obtaining high surface area PtCo/C intermetallic catalysts for improved PEM fuel cell performance, RSC. Adv. 13 (2023) 4601–4611, https://doi.org/10.1039/D2RA07780A.

[29] L. Pavko, M. Gatalo, G. Križan, J. Križan, K. Ehelebe, F. Ruiz-Zepeda, M. Šala, G. Dražić, M. Geuß, P. Kaiser, M. Bele, M. Kostelec, T. Đukić, N. Van de Velde, I. Jerman, S. Cherevko, N. Hodnik, B. Genorio, M. Gaberšček, Toward the continuous production of multigram quantities of highly uniform supported metallic nanoparticles and their application for synthesis of superior intermetallic Pt-alloy ORR electrocatalysts, ACS. Appl. Energy Mater. 4 (2021) 13819–13829, https://doi.org/10.1021/acsaem.1c02570.

[30] D.C. Marcano, D.V. Kosynkin, J.M. Berlin, A. Sinitskii, Z.Z. Sun, A. Slesarev, L. B. Alemany, W. Lu, J.M. Tour, Improved synthesis of graphene oxide, ACS. Nano 4 (2010) 4806–4814, https://doi.org/10.1021/nn1006368.

[31] A. Kongkanand, High-Activity Dealloyed Catalysts, General Motors LLC, Warren, MI (United States), United States, 2014, p. 180, https://doi.org/10.2172/1262711. Medium: ED; Size.

[32] M. Prokop, P. Capek, M. Vesely, M. Paidar, K. Bouzek, High-temperature PEM fuel cell electrode catalyst layers part 2: experimental validation of its effective transport properties, Electrochim. Acta 413 (2022), https://doi.org/10.1016/j.electacta.2022.140121.

[33] P. Bindra, S.J. Clouser, E. Yeager, Platinum dissolution in concentrated phosphoric acid, J. Electrochem. Soc. 126 (1979) 1631, https://doi.org/10.1149/1.2129345.

[34] T. Soboleva, X. Zhao, K. Malek, Z. Xie, T. Navessin, S. Holdcroft, On the micro-, meso-, and macroporous structures of polymer electrolyte membrane fuel cell catalyst layers, ACS. Appl. Mater. Interfaces. 2 (2010) 375–384, https://doi.org/10.1021/am900600y.
[35] Y. Oono, A. Sounai, M. Hori, Influence of the phosphoric acid-doping level in a polybenzimidazole membrane on the cell performance of high-temperature proton exchange membrane fuel cells, J. Power. Sources. 189 (2009) 943–949, https://doi.org/10.1016/j.jpowsour.2008.12.115.
[36] K. Kwon, J.O. Park, D.Y. Yoo, J.S. Yi, Phosphoric acid distribution in the membrane electrode assembly of high temperature proton exchange membrane fuel cells, Electrochim. Acta 54 (2009) 6570–6575, https://doi.org/10.1016/j.electacta.2009.06.031.
[37] N. Bevilacqua, T. Asset, M.A. Schmid, H. Markötter, I. Manke, P. Atanassov, R. Zeis, Impact of catalyst layer morphology on the operation of high temperature PEM fuel cells, J. Power Sources Adv. 7 (2021) 100042, https://doi.org/10.1016/j.powera.2020.100042.
[38] G. Liu, H. Zhang, J. Hu, Y. Zhai, D. Xu, Z.-g. Shao, Studies of performance degradation of a high temperature PEMFC based on H3PO4-doped PBI, J. Power. Sources. 162 (2006) 547–552, https://doi.org/10.1016/j.jpowsour.2006.07.008.
[39] A. Orfanidi, M.K. Daletou, L. Sygellou, S.G. Neophytides, The role of phosphoric acid in the anodic electrocatalytic layer in high temperature PEM fuel cells, J. Appl. Electrochem. 43 (2013) 1101–1116, https://doi.org/10.1007/s10800-013-0626-2.
[40] Q. He, B. Shyam, M. Nishijima, D. Ramaker, S. Mukerjee, Mitigating phosphate anion poisoning of cathodic Pt/C catalysts in phosphoric acid fuel cells, J Phys. Chem. C 117 (2013) 4877–4887, https://doi.org/10.1021/jp309282n.
[41] M. Prokop, T. Bystron, P. Belsky, O. Tucek, R. Kodym, M. Paidar, K. Bouzek, Degradation kinetics of Pt during high-temperature PEM fuel cell operation part III: voltage-dependent Pt degradation rate in single-cell experiments, Electrochim. Acta 363 (2020), https://doi.org/10.1016/j.electacta.2020.137165.
[42] S. Rasouli, D. Myers, N. Kariuki, K. Higashida, N. Nakashima, P. Ferreira, Electrochemical degradation of Pt–Ni nanocatalysts: an identical location aberration-corrected scanning transmission electron microscopy study, Nano Lett. 19 (2019) 46–53, https://doi.org/10.1021/acs.nanolett.8b03022.
[43] T. Dukic, L.J. Moriau, L. Pavko, M. Kostelec, M. Prokop, F. Ruiz-Zepeda, M. Sala, G. Drazic, M. Gatalo, N. Hodnik, Understanding the crucial significance of the temperature and potential window on the stability of carbon supported Pt-alloy nanoparticles as oxygen reduction reaction electrocatalysts, ACS. Catal. 12 (2022) 101–115, https://doi.org/10.1021/acscatal.1c04205.
[44] M. Gatalo, P. Jovanovič, U. Petek, M. Šala, V.S. Šelih, F. Ruiz-Zepeda, M. Bele, N. Hodnik, M. Gaberšček, Comparison of Pt–Cu/C with benchmark Pt–Co/C: metal dissolution and their surface interactions, ACS. Appl. Energy Mater. 2 (2019) 3131–3141, https://doi.org/10.1021/acsaem.8b02142.
[45] J. Chivot, L. Mendoza, C. Mansour, T. Pauporté, M. Cassir, New insight in the behaviour of Co–H2O system at 25–150°C, based on revised Pourbaix diagrams, Corros. Sci. 50 (2008) 62–69, https://doi.org/10.1016/j.corsci.2007.07.002.
[46] K. Hayashi, T. Tomimori, Y. Chida, N. Todoroki, T. Wadayama, Hydrogen peroxide generation and Hydrogen oxidation reaction on Pt/Co/Pt(111) and Pt/Co/Pt(100) single-crystal model catalyst surface, ACS. Catal. 14 (2024) 14069–14077, https://doi.org/10.1021/acscatal.4c03106.
[47] M.K. Daletou, M. Geormezi, E. Vogli, G.A. Voyiatzis, S.G. Neophytides, The interaction of H3PO4 and steam with PBI and TPS polymeric membranes. A TGA and Raman study, J. Mater. Chem. A 2 (2014) 1117–1127, https://doi.org/10.1039/C3TA13335D.